ENCIT2024

20th Brazilian Congress of Thermal Sciences and Engineering

ABCM
Associação Brasileira de Engenharia e Ciências Mecânicas

20th Brazilian Congress of Thermal Sciences and Engineering
November 10th–14th, 2024, Foz do Iguaçu - PR - Brazil

ENC-2024-0321
Detailed Model & Experimental Validation of a Flat Solar Collector

Renzo Guido Cruz
Pedro Galione Klot
Facultad de Ingeniería, Universidad de la República, Montevideo, Uruguay
rguido@fing.edu.uy - pgalione@fing.edu.uy

Juan Manuel Rodriguez Muñoz
Centro Universitario Regional Norte, Universidad de la República, Salto, Uruguay
jrodrigue@fing.edu.uy

Abstract. This work presents a comprehensive model of a commercially available flat-plate solar collector, including risers and headers, simulated using a custom-developed Python program. The program models each component of the collector, incorporating physical effects often neglected in other computational models but crucial for accurately predicting temperature profile changes at a sub-minute time scale. The flat-plate solar collector model employs a multi-node temperature arrangement, discretized along the horizontal or vertical axes. Each node consists of four temperatures: one for the glass cover, one for the aluminum casing, one for the absorber plate's junction with the copper tubes, and one for the working fluid. The simulations were validated against experimental measurements conducted at a testing facility adhering to ISO 9806 standards, showing excellent agreement between simulation results and experimental data. The comparisons included data from three subtests: performance, incident angle modifier, and effective thermal capacity, all part of the steady-state testing method prescribed by the standard. All three subtests showed strong qualitative and quantitative agreement, with all parameters falling within the range of experimental uncertainty.

Keywords: Solar Collector, Thermal Energy, Transient Thermal Analysis, Flat Plate Solar Collector

1. INTRODUCTION

Solar thermal energy is a sustainable method for providing domestic hot water and can also be an attractive investment for families looking to reduce their energy bills. The most popular thermal energy system for domestic hot water is flat-plate solar collectors, which use sunlight to heat water and store it in storage tanks. An overview of different types of solar thermal technologies can be found in (Kalogirou, 2004), which discusses flat-plate solar collectors. The present work focuses on the detailed modeling of a commercially available flat-plate solar collector, including headers and risers (Baroni GRAS 200100). Numerical simulations were performed to solve the complex heat exchange and thermal analysis, separating each component and simulating them using a custom-developed Python program.

The program aims to physically model each part of the collector, considering effects usually neglected by other computational models but necessary to predict temperature profile changes on a minute-by-minute scale accurately. The flat-plate solar collector model uses a multi-node temperature arrangement, discretized along the horizontal or vertical axes, with four temperatures in each node: one for the glass cover, one for the aluminum casing, one for the absorber plate, and one for the fluid inside. The first transient models, which used one or two nodes to account for the thermal capacity of the collector, as seen in (Klein *et al.*, 1974) or (Hilmer *et al.*, 1999), were qualitatively better than zero-node models but still fell short of truly capturing the dynamics of the solar collector. The 4D arrangement used in this work is uncommon in flat-plate solar collector literature, where the 3D arrangement without simulating the casing is more popular, as seen in (Plantier *et al.*, 2003) or (Jiandong *et al.*, 2015), and is found in many studies. A similar four-dimensional model was developed by (Kamminga, 1985), where the insulator was simulated as a node instead of the aluminum casing. However, most previous works focus on the collector's response to partially cloudy days, where processes occur on the order of tens of minutes. We found that capturing the dynamic behavior of the collector required some modifications to the physical model.

The paper is structured as follows. Section 2 describes the physical model of the flat-plate collector, presenting the energy balance equations, the parameters used, and the discretization of the model into finite elements. Additionally, a glass transmissivity test is introduced, from which properties as a function of angle are obtained. Section 3 outlines the three tests conducted on these collectors according to the standard and the procedures followed. Section 4 compares the experimental and simulation results for the three tests. The article concludes with a concise summary of the findings.

2. PHYSICAL & NUMERICAL MODEL

2.1 Physical model

The physical model was inspired by the detailed work of Duffie *et al.* (2020) and the article by (Plantier *et al.*, 2003), with several crucial additions to better capture behavior over short periods. The most significant changes include the addition of an extra temperature node in the aluminum casing and axial heat conduction, which accounts for heat transfer along the riser tubes and the conduction exchange between these tubes and the lower and upper headers. The model used is four-dimensional, resolving the temperature profile for the copper tubes, the fluid circulating inside them, the glass cover, and the aluminum casing. A schematic of the finite element simulation is shown in Fig. 1. The assumptions of the model are as follows:

1. The aluminum plate can be modeled with the temperature profile of a fin, with the copper temperature at the base.

2. The insulation is perfect on the lateral walls of the casing.

3. Because the risers are much longer than the headers, the flow distribution in the risers is assumed to be uniform.

4. Each finite element of glass and casing only exchanges heat in the vertical direction.

5. The convective heat exchange coefficients are uniform across the absorber and the glass cover.
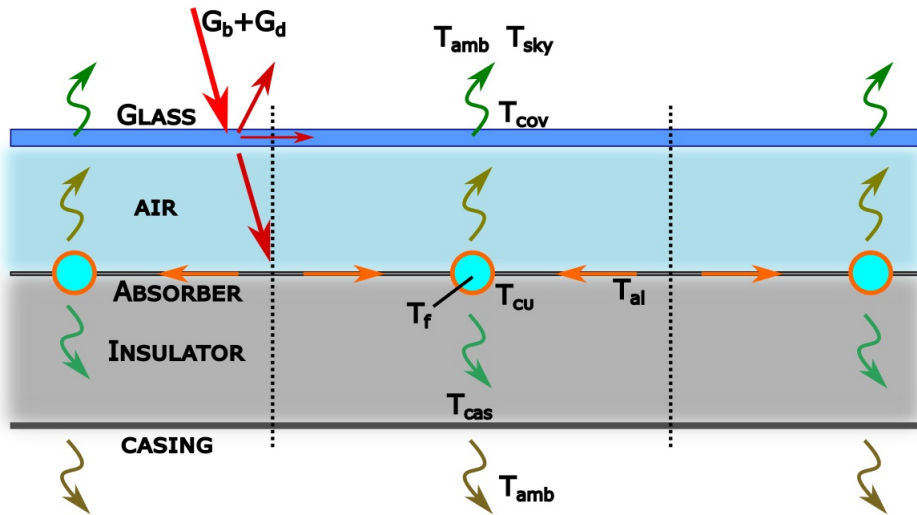

Figure 1: Scheme of a finite element of the collector. In the axial dimension, each part has a length dy.

With the above assumptions, the energy balance equations can be written. Equation (1) shows the energy balance equation for a differential fluid element.

$$\rho_w A_w dy c_w \dot{T}_f = h_f D \pi dy (T_{cu} - T_f) - \dot{m} c_w (T_f^{out} - T_f^{in}) \tag{1}$$

Where h_f is the heat transfer coefficient inside the tubes, ρ is the density, A is the section normal to the flow, dy is the length of the vertical step, c is the specific heat capacity, D is the inner diameter of the pipe. The sub-index w means that the properties are those of water.

The energy balance for an absorber element is shown in Eq. (2), where an equivalent mass and combined thermal capacity C_{abs} between the aluminum fins and copper tubes are used.

$$C_{abs} \dot{T}_{cu} = S_{abs} A - \frac{\kappa_{ins}}{e_{ins}} A (T_{eq} - T_{cas}) - h_{cav} A (T_{eq} - T_{cov}) - h_f D \pi dy (T_{cu} - T_f) + \kappa_{eq} dy A_{eq} \Delta T \tag{2}$$

Here, T_{eq} refers to the mean temperature of both the copper tube and the fin profile, S_{abs} is the absorbed solar radiation per unit area, A is the area of the finite element of the absorber and the copper tubes, κ_{ins} and e_{ins} are the thermal conductivity and thickness of the insulator, respectively.

The aluminum temperature is not simulated independently; instead, a fin profile is assumed with the copper base temperature and an adiabatic end halfway between the tubes. Other terms with the subscript eq also represent properties of both materials combined. The h_{cav} heat transfer coefficient used is taken from Jiandong *et al.* (2015), where small convection cells are generated within the tubes.

The third energy balance in the four-dimensional model is for a glass volume element, presented in Eq. (3), which includes a heat exchange term with the absorber plate, a solar radiation absorption term, and two terms for losses to the environment by convection and radiation.

$$\rho_g dV_g c_g \dot{T}_g = h_{cav} A_g (T_{eq} - T_{cov}) + S_g A_g - h_{cf} A_g (T_{cov} - T_{amb}) - h_{rad} A_g (T_{cov} - T_{sky}) \tag{3}$$

Where the subscript g refers to the glass properties, dV_g refers to a small volume of glass, S_g to the power per unit area absorbed by glass, which is modeled in Section 2.4, and h_{cf} and h_{rad} are the forced convection and radiation heat transfer coefficients, respectively.

The last energy balance is for a small casing volume, shown in Eq. (4). Including the aluminum casing as an independent node is uncommon for this type of analysis. The casing warms up due to the absorber plate above the glass wool and loses heat to the environment. The thickness of the aluminum in the casing is 0.8 mm, and it weighs almost 6 kg, so its contribution to the overall heat capacity is not negligible. Conduction in the casing was not considered due to the time required to compute bi-dimensional heat conduction and the assumption that it exchanges heat with T_{eq}. The glass wool heat capacity was split in half, increasing both the absorber heat capacity and the casing heat capacity.

$$\rho_{al} A_{cas} dy c_{al} \dot{T}_{cas} = \frac{\kappa_{ins}}{e_{ins}} A_{cas} (T_{eq} - T_{cas}) - h_{cf} A_{cas} (T_{cas} - T_{amb}) \tag{4}$$

Where the subscript cas indicates the properties are those of the aluminum casing.

Solving these equations revealed that axial heat conduction in the upper header is key to reproducing the transient thermal behavior. Additionally, the efficiency of the aluminum fins was considered variable, as their temperature profile (and consequently, heat losses) changes with temperature and solar radiation. The casing temperature was included in the model to improve precision during quick transitions.

2.2 Relevant parameters

Table 1 shows all the relevant parameters taken from different authors. The metal properties were taken from Bergman *et al.*, 2011 and the absorptivities and emissivities were given in the collector's datasheet. As for the convective transfer coefficients, many works cited in the table had empirical formulas to adjust the coefficient.

Table 1: References: [R1]Bergman *et al.*, 2011; [R2]Sartori, 2006; [R3]Li *et al.*, 2017.

Parameter	Value or Formula
κ_{al}; c_{al}; ρ_{al}	$170\ Wm^{-1}K^{-1}$; $875\ Jkg^{-1}K^{-1}$; $2770\ kg^1m^{-3}$
κ_{cu}; c_{cu}; ρ_{cu}	$385\ Wm^{-1}K^{-1}$; $390\ Jkg^{-1}K^{-1}$; $8960\ kg^1m^{-3}$
h_f [R1]	$\frac{\kappa}{D} 0.17 Re^{0.33} Pr^{0.43} Gr^{0.1} (Pr/Pr_w)^{0.25}$. Laminar flow.
h_{cav}	$\alpha_0 |T_{abs} - T_{cov}|^n$. $\alpha_0 = 1.4 - \frac{\beta}{139}$ and $n = 0.28 + \frac{\beta}{1250}$.
h_{cf} [R2]	$0.037 Re^{0.8} Pr^{0.33} \kappa L^{-1}$
h_{rad}	$\epsilon\ \sigma\ (T_1^2 + T_2^2)(T_1 + T_2)(\frac{1}{\epsilon_{cu}} + \frac{1}{\epsilon_{cov}} - 1)^{-1}$
ϵ_{abs}	0.25 from collector's Data-sheet
ϵ_{glass}	0.9 from collector's Data-sheet
α_{abs}	0.86 from collector's Data-sheet
T_{sky} [R3]	$\epsilon_{sky}^{0.25} T_{amb}$ with $\epsilon_{sky} = c_1 + c_2 P_v \exp(\frac{c_3}{T_{amb}})$.
	$c_1 = 0.685$, $c_2 = 3.2 \times 10^{-5} Pa^{-1}$, $c_3 = 1699K$.
P_v	$0.6\ 6.1094 \exp(17.625 \frac{T_{amb} - 273}{T_{amb} - 30.11})$

Some of the parameters were modified from their original values. Due to numerical issues, the simulated area of the glass was 1.95 m², although the actual area of the glass is 2.05 m², which is 5.1% larger. To correct this discrepancy, the thermal capacity of the glass and the heat exchange coefficients were also increased by 5.1%. This correction assumes that the non-simulated parts of the glass will have a similar temperature and heat exchange behavior as the rest of the glass. The same correction was applied to the aluminum casing and the glass wool.

Moreover, the density of the aluminum fins was modified due to overlapping aluminum sheets in several places. Fins with double sheets will exhibit different dynamic behavior compared to those without, depending significantly on where the aluminum sheet is folded. To maintain a detailed global model without excessive complexity, the density of the aluminum was artificially increased to estimate the added thermal capacity of the absorber.

2.3 Discretization

Small elements were considered to solve the equations discretely, where each riser tube was independently resolved and divided into 65 small segments, defining a spatial step for the tube. The time step was chosen to ensure that the

fluid flow through the riser tubes was close to the Courant number condition of 1, minimizing numerical diffusion in the primary heating region of the water in the collector. Once the time and spatial steps were defined, the temporal and spatial derivatives could be discretized. For the inlet temperature of an element, the temperature of the previous element was used, and for the outlet temperature, the temperature of the element itself was taken. In the headers, velocity drops or increases due to the constant pipe section and varying flow rate. This leads to some numerical diffusion in the headers; however, since the headers are less critical than the risers, this small diffusion error is considered negligible.

The method for solving the equations was implicit for the copper tubes and explicit for the water, glass, and casing. To avoid excessively long computation times when solving for the temperature in the copper tubes, the Thomas algorithm for solving tridiagonal matrices was implemented. Numerical diffusion occurs in the headers due to changes in fluid velocity within the constant section of the header, caused by decreasing or increasing flow rates.

The length of the volume in the risers was $\Delta y = 29.8$ mm, dividing the risers into 65 small steps. The time step Δt used in all the simulations was near 0.36 s, which was selected so the Courant number in the riser tubes was 1. To prove the convergence of the solution with these parameters, the spatial and time steps were halved, and the solutions were compared. The difference was less than one in a thousand, indicating that the selected time steps are small enough to consider the solution converged.

2.4 Glass modeling & test

The Incident Angle Modifier (IAM) is usually defined experimentally for solar collectors because it encompasses the effects of changes in the transmissivity of the cover, changes in the absorptivity of the selective coating, and the shadows cast by different parts of the collector. In this work, we aimed to develop and validate a model for the glass transmissivity as a function of the angle of incidence. An experiment was conducted in which the incident irradiance was measured both behind and in front of the glass of a Baroni collector. Two Kipp & Zonen class A pyranometers were used for the measurements, one positioned behind the glass and the other in front of it. The ratio between these two measurements represents the instantaneous transmissivity of the glass and any dust deposited on it.

The proposed model to fit the experimental data separates the reflection due to the change in medium from the reflection caused by dust on the glass surface. The reflectivity of light entering a new medium with a different refraction index is described by Snell's Law.

Equation (5) shows the model used to describe the absorption of the electromagnetic wave in the glass. The transmittance was obtained as the difference between the incident, absorbed, and reflected intensities. To solve the system, it was considered that there are two boundaries between media, one air-glass and the other glass-air. A more detailed analysis can be found in (Griffiths, 2023).

$$\alpha_{vid} = 1 - \exp\left[-k_{ext}\frac{e}{\cos(\theta_2)}\right] \tag{5}$$

Additionally, it was necessary to add a linear term to the reflectivity due to the dirt on the glass, as presented in Eq. (6).

$$R_m = p_0 - p_1 \cos(\theta_1) \tag{6}$$

These two equations contain three unknown parameters that were fit using the available experimental data: the extinction coefficient of the glass (k_{ext}), which is expected to be between 8 and 20 m^{-1}, and p_0 and p_1, which are calculated to fit the data. $p_0 - p_1$ is expected to range between 0 and 0.05, according to the works by (Hegazy, 2001) and (Said and Walwil, 2014) for a 45-degree tilt angle exposed to dust for less than a week. Figure 2 shows the experimental data and the fitted function using the least squares method. The values obtained for the fitted parameters are $k_{ext} = 12m^{-1}$, $p_0 = 0.155$, and $p_1 = 0.127$, which aligns with the expected values. The model demonstrates excellent performance in explaining the experimental data.

It is expected that the absorptivity of the absorber plate will not change significantly until the incidence angle approaches $40°$. Additionally, due to the collector's geometry, the edges will not cast any shadows on the absorber for incidence angles smaller than $50°$. Since the evaluated incidence angles are all smaller than $60°$, it is assumed that any change in the optical efficiency of the collector is exclusively due to variations in the glass transmittance. This hypothesis is further discussed later in the article.

3. EXPERIMENTAL TEST

3.1 Experimental facilities

To validate the numerical model, tests were conducted on a commercial solar collector at the solar collector test bench located in Salto, Uruguay (Lat: -31.28°, Long: -57.92°). The test bench is designed to operate according to the ISO-9806 (2017) standard, allowing for performance tests, incident angle modifier index tests, and thermal capacity tests to
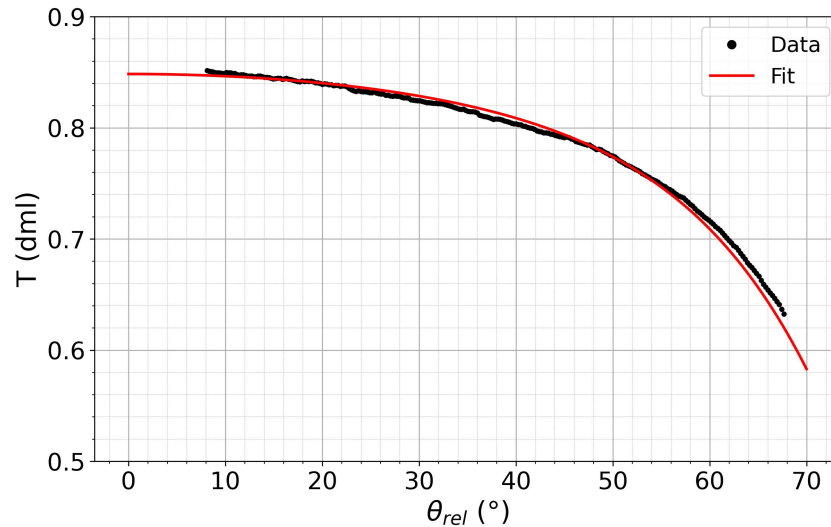
Figure 2: Comparison of the experimental data and the model with fitted parameters.

determine the characteristic curve of the collector. The test bench consists of a platform capable of tilting to any desired angle with a north orientation, two three-wire PT100 thermocouples for measuring the water temperature, and an Endress & Hauser electromagnetic flowmeter with an uncertainty of 0.5% of the measurement. For solar radiation measurements, two Kipp & Zonen pyranometers (CMP 10 and CMP 11), class A, were used to measure the horizontal and inclined total irradiance. Another Kipp & Zonen pyranometer (CMP 6), class B, with a shading band, was used to measure the diffuse component of the incident irradiance. A correction factor for the measurement due to the shading band is provided in the datasheet of the pyranometer. A more detailed explanation of the test bench components can be found in (Rodríguez-Muñoz *et al.*, 2021).

3.2 Methodology

The testing standard ISO-9806 (2017) proposes two methodologies: Steady State Testing (SST) and Quasi-Dynamic Testing (QDT). In this work, the measurement sequences from the SST methodology were used to verify the numerical model. It is important to note that there are three independent subtests: (i) the performance test, (ii) the incident angle modifier test, and (iii) the effective thermal capacity test. The numerical model was then executed under the same climatic and usage conditions, and the results were compared with the experimental measurements (useful power or outlet temperature of the collector). The subtests of the SST method are described below.

In the first test, the useful power must be measured for four different inlet temperatures. For each inlet temperature, four independent points must be measured, resulting in a total of 16 points. Each point consists of an average over a determined measurement period, such as 10 minutes, during which all required stability conditions are met. The measurements should be taken with small incidence angles (i.e., near-normal incidence).

For the second test (IAM determination), useful power measurements are taken at various incidence angles between $40°$ and $70°$. For each measurement period, an inlet temperature should be imposed such that the mean fluid temperature is as close as possible to the ambient temperature.

The effective thermal capacity test was conducted according to section 25.2 of the ISO 9806 standard. At the beginning of the test, the inlet temperature was set equal to the ambient temperature, and the collector was covered with a reflective blanket to reach a steady state. The cover was then removed, allowing the collector to reach a new steady-state point, which differed from the initial one due to the effect of solar irradiance. This test was also performed with normal incidence, meaning small incidence angles.

4. RESULTS

4.1 Performance test

The first test performed on the solar collector was an efficiency test according to the standard. The collector's performance was measured and compared with the simulation on a clear day. In Fig. 3, the comparison of the efficiency as a function of reduced temperature between the experimentally obtained curve (solid black curve) and the simulated curve (dashed red curve) is shown. It can be seen that the simulated curve is similar to the experimental curve, although it appears to have a slightly lower curvature. The incident irradiation for the experimental and simulated curves was the same, around $1075 \ W/m^2$, with a small diffuse fraction typical of a clear day, between 7% and 9%. The ambient temperature

ranged between 26°C and 29°C. As for the efficiency's uncertainty, the most relevant uncertainty in the measurements was the one from the pyranometer, which is around 3 to 6% for all angles, leading to a similar uncertainty in each point measured.
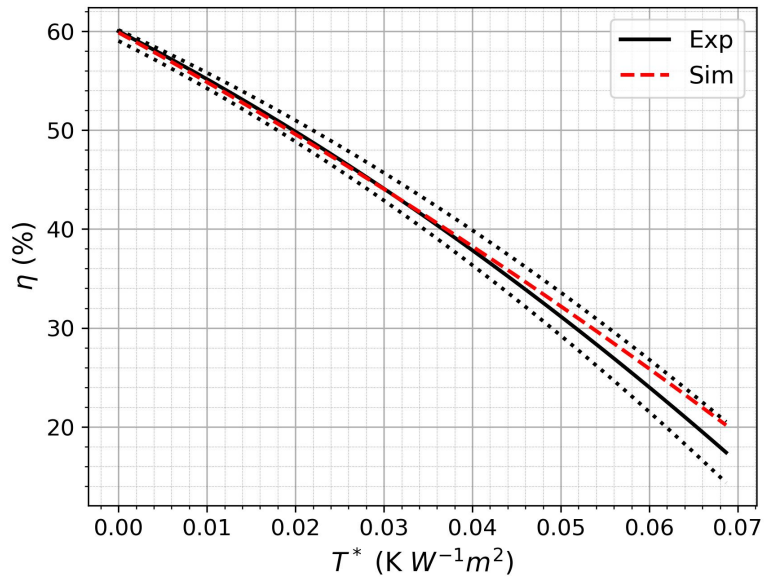

Figure 3: Comparison of the experimental and simulated efficiency as a function of the reduced temperature T^*. The pointed lines represent the statistical uncertainty in the experimental fitted curve.

4.2 Incident Angle Modifier test

The simulation was also compared throughout the day with the Incident Angle Modifier (IAM) subtest. The angular dependence of the collector's optical performance is highly sensitive to variables that are difficult to measure, such as the absorptivity of the selective coating depending on the angle, the reflectivity and transmissivity of the glass, the dirt on the glass, and the shadows produced on the absorber. It was assumed that the most relevant phenomenon is glass transmissivity, which was the only one considered in the model. Fig. 4 shows the comparison between the water outlet temperature in the simulation and the test bench for the same input data throughout an entire day. It can be seen that an almost perfect correlation was achieved between the experimental data and the simulation.
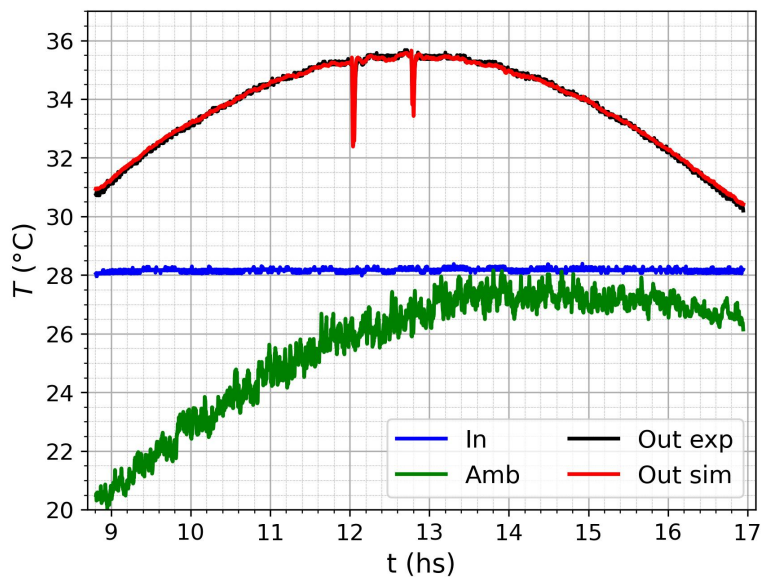

Figure 4: Comparison of the experimental and simulated collector behavior with the same inputs. The fall in the output temperature was due to a cloud passing by. The uncertainty of the measurements is not represented, nevertheless, the testing standard requires less than 0.1 K uncertainties in the temperature.

The useful heat was calculated both experimentally and through simulations to measure the differences between the red and black curves. The percentage difference between these values was determined by comparing it to the experimental useful heat value. Figure 5 shows the percentage difference as a function of the incidence angle. On the one hand, the uncertainty in the experimental useful heat is associated with the uncertainties in the flow meter and the outlet and inlet temperatures. The relative experimental uncertainty is represented by a dotted black curve for different angles. On the other hand, the uncertainty in the simulation results is tied to the uncertainty in the solar irradiance measured by Kipp & Zonen class A pyranometers, which is estimated to be less than $\pm 3\%$ for near-normal angles and up to $\pm 6\%$ for larger angles. The relative uncertainty of the model's output heat was validated (by simulating with $\pm 6\%$ irradiation) to be almost the same as the pyranometer's uncertainty. As a result, the difference between the model and the experimental results falls within the same range as the uncertainty in solar measurements.

A difference is expected due to the angular dependence of the plate's absorptivity and emissivity, which begin to change significantly for angles greater than $40°$, as well as the inherent shadows cast by the collector. It is observed that there is almost zero systematic error between the simulated and experimental results for angles smaller than $30°$ or $40°$, with the difference increasing up to 8% for angles approaching $60°$. From the shape of the difference curve, ΔQ_{use}, it can be argued that these changes in the absorber's properties, along with the shading effects, account for the observed systematic discrepancy at larger angles.

The figure also includes a scatter plot comparing the simulated and experimental heat. It can be visually observed that the dispersion is extremely low. Performance indicators were used to quantify the dispersion. One of these indicators is the relative difference between the experimental and simulated useful heat for angles less than $40°$, which is -0.2%, indicating that the simulated useful heat is slightly lower than the experimental value. However, this difference is smaller than the uncertainty of the instruments used. For angles greater than $50°$, the relative difference is 3.0%. Another important performance indicator is the relative mean squared difference; its value for angles smaller than $40°$ is 0.7%, and 3.6% for angles greater than $50°$.
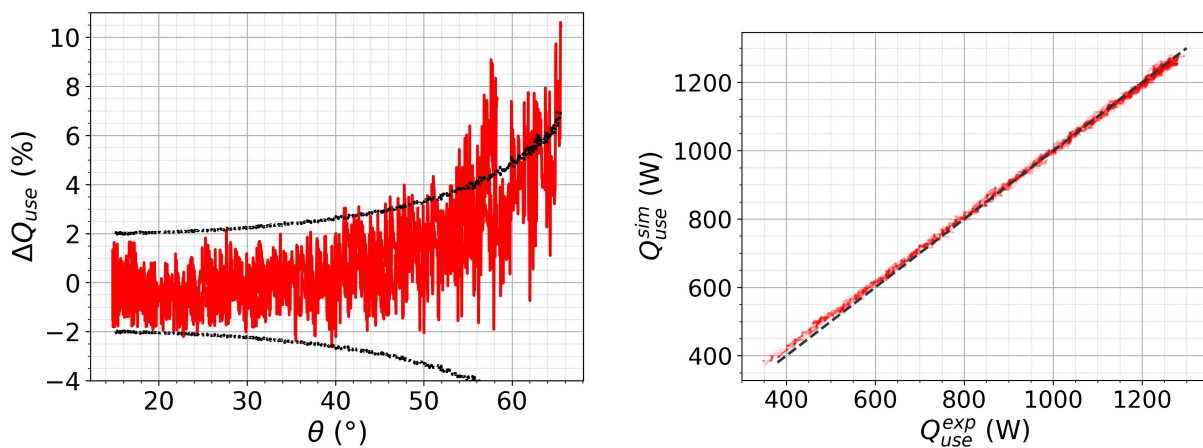

Figure 5: In the left panel, the difference between the experimental and simulated useful heat extracted from the collector is shown as a function of the relative angle between the collector and the sun. The black dotted line is the experimental relative uncertainty. The right panel shows the scatter plot comparing simulated and experimental useful heat.

4.3 Effective thermal capacity test

The last test performed on the solar collector was a thermal capacitance test. In this test, water enters the solar collector at a constant rate, but a blanket covers the absorber, rendering the inlet radiation negligible. At a given moment, the blanket is removed, and the collector absorber perceives a step input in solar radiation. Figure 6 shows the evolution of the inlet, outlet, and ambient temperatures after the blanket is removed at time $t = 0$. A small difference can be observed between the simulated outlet temperature (in red) and the measured outlet temperature (in black) for the same inlet and ambient temperatures and the same solar irradiation.

From this test, the thermal capacitance of the flat-plate collector was calculated. In the simulation, the thermal capacity per gross area was 12.9 kJ kg^{-1} m^{-2}, while the experimental data showed a capacity of (13.3 ± 0.6) kJ kg^{-1} m^{-2}. The relative uncertainty of the experimental value is less than 5%, primarily due to uncertainties in the initial and final times. The time uncertainty was set to half the time sampling period, 5 seconds. The simulated capacity falls within the experimental uncertainty range, indicating strong agreement between the two. The characteristic time for the system to reach thermal equilibrium was 165 seconds in the simulation and (158 ± 7) seconds in the experiment. The simulated value is within the expected range, as seen by comparing the red and black curves, which reach steady-state values at similar times.
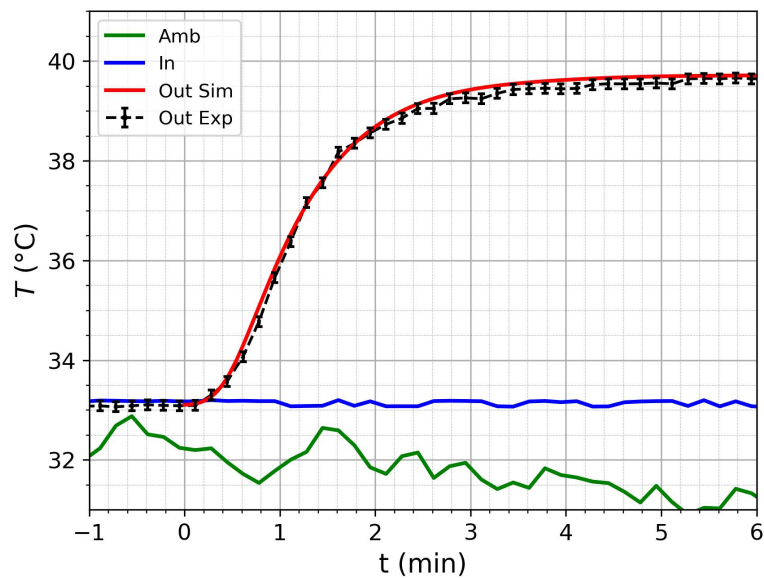
Figure 6: Comparison of the experimental and simulated transient behavior.

By resolving all temperature nodes in the simulation, the energy stored in each component can be examined, revealing their contributions to the overall thermal capacity. Compared to others, a key contribution of this work is the inclusion of the upper header in the simulation, which accounts for 9.0% of the collector's thermal capacity. In contrast, the lower header contributes only 0.5% of the stored sensible energy and could have been neglected for this type of transient analysis. Another important improvement was modeling the aluminum casing and distributing the thermal capacity of the glass wool between the casing and the absorber plate, which added 11% to the collector's total thermal capacity. Additionally, accounting for the fact that some of the aluminum fins were doubled contributed an extra 10%. Without these modifications, the simulated thermal capacity of the collector would be approximately half of the experimentally obtained value.

Furthermore, incorporating these detailed components into the model allows a more accurate representation of the collector's dynamic behavior, especially during rapid transients.

5. CONCLUSIONS

In summary, the model demonstrates excellent performance in both efficiency and IAM tests. No angular correction is required for incident angles smaller than 40°, though empirical corrections are necessary for larger angles. Changes in glass transmissivity are sufficient to account for variations in thermal output throughout most of the day. The mean bias difference between the simulated and actual useful heat for small incident angles is −0.2%, with a root mean squared difference of 0.7%, suggesting that the differences between the model and the experiments are due to random measurement errors, with no evidence of systematic error. For incident angles greater than 50°, these differences increase to 3.0% and 3.6%, respectively, indicating larger systematic deviations. This was expected, as the model does not account for changes in absorptivity or shading effects. Nevertheless, these differences are of the same order as the experimental measurement uncertainty.

For the thermal capacity test, the simulated and experimental output temperatures show excellent quantitative and qualitative agreement. The simulated thermal capacity value falls within the experimental uncertainty range, and the time required by the simulation to reach thermal equilibrium is also within this range.

6. ACKNOWLEDGEMENTS

7. REFERENCES

Bergman, T.L., Lavine, A.S., Incropera, F.P. and DeWitt, D.P., 2011. *Introduction to heat transfer*. John Wiley & Sons.
Duffie, J.A., Beckman, W.A. and Blair, N., 2020. *Solar engineering of thermal processes, photovoltaics and wind*. John Wiley & Sons.
Griffiths, D.J., 2023. *Introduction to electrodynamics*. Cambridge University Press.

Hegazy, A.A., 2001. "Effect of dust accumulation on solar transmittance through glass covers of plate-type collectors". *Renewable energy*, Vol. 22, No. 4, pp. 525–540.

Hilmer, F., Vajen, K., Ratka, A., Ackermann, H., Fuhs, W. and Melsheimer, O., 1999. "Numerical solution and validation of a dynamic model of solar collectors working with varying fluid flow rate". *Solar Energy*, Vol. 65, No. 5, pp. 305–321.

ISO-9806, 2017. "Solar energy – solar thermal collectors – test methods". Standard, International Organization of Standarization, Switzerland.

Jiandong, Z., Hanzhong, T. and Susu, C., 2015. "Numerical simulation for structural parameters of flat-plate solar collector". *Solar Energy*, Vol. 117, pp. 192–202.

Kalogirou, S.A., 2004. "Solar thermal collectors and applications". *Progress in energy and combustion science*, Vol. 30, No. 3, pp. 231–295.

Kamminga, W., 1985. "The approximate temperatures within a flat-plate solar collector under transient conditions". *International journal of heat and mass transfer*, Vol. 28, No. 2, pp. 433–440.

Klein, S., Duffie, J. and Beckman, W., 1974. "Transient considerations of flat-plate solar collectors".

Li, M., Jiang, Y. and Coimbra, C.F., 2017. "On the determination of atmospheric longwave irradiance under all-sky conditions". *Solar Energy*, Vol. 144, pp. 40–48.

Plantier, C., Fraisse, G. and Achard, G., 2003. "Development and experimental validation of a detailed flat-plate solar collector model". In *ISES solar world congress*.

Rodríguez-Muñoz, J.M., Bove, I. and Alonso-Suárez, R., 2021. "Novel incident angle modifier model for quasi-dynamic testing of flat plate solar thermal collectors". *Solar Energy*, Vol. 224, pp. 112–124. ISSN 0038-092X. doi:https://doi.org/10.1016/j.solener.2021.05.026.

Said, S.A. and Walwil, H.M., 2014. "Fundamental studies on dust fouling effects on pv module performance". *Solar Energy*, Vol. 107, pp. 328–337.

Sartori, E., 2006. "Convection coefficient equations for forced air flow over flat surfaces". *Solar energy*, Vol. 80, No. 9, pp. 1063–1071.

8. RESPONSIBILITY NOTICE

The authors are solely responsible for the printed material included in this paper.